Energy Storage Materials 34 (2021) 629–639

Contents lists available at ScienceDirect

Energy Storage Materials

journal homepage: www.elsevier.com/locate/ensm

In situ formation of poly(butyl acrylate)-based non-flammable elastic quasi-solid electrolyte for dendrite-free flexible lithium metal batteries with long cycle life for wearable devices

Guodong Zhou[a], Xidong Lin[a], Jiapeng Liu[a], Jing Yu[a], Junxiong Wu[a], Ho Mei Law[a], Zheng Wang[a], Francesco Ciucci[a,b,*]

[a] Department of Mechanical and Aerospace Engineering, The Hong Kong University of Science and Technology, Clear Water Bay, Hong Kong, China
[b] Department of Chemical and Biological Engineering, The Hong Kong University of Science and Technology, Clear Water Bay, Hong Kong, China

ARTICLE INFO

Keywords:
Non-flammable elastic quasi-solid electrolyte
In situ polymerization
Poly(butyl acrylate) flexible batteries

ABSTRACT

With the rapid development of wearable devices, there is an increasing demand for ultra-safe flexible lithium-ion batteries (LIBs) capable of delivering high energy density. Because it can provide the highest possible capacity of 3860 mAh g^{-1}, lithium metal has drawn tremendous research attention. However, Li is a highly reactive metal that grows dendrites during the cycling of lithium-metal batteries (LMBs). To resolve the problem, we developed a new non-flammable elastic quasi-solid electrolyte (QSE), which can be polymerized in situ and whose composition is tailored to achieve high elasticity. Moreover, the incorporation of trimethyl phosphate (TMP) renders the electrolyte non-flammable. Thanks to the solid electrolyte interphase (SEI) formed, the LMB with QSE displays excellent cycling stability as it can be operated for 500 cycles, with a capacity retention of 94%. The corresponding symmetric cell cycled stably for more than 500 h. Scanning electron microscopy (SEM) and density functional theory (DFT) calculations reveal that fluoroethylene carbonate (FEC) is critical in forming the LiF-rich SEI that enables long-term cycling stability. In brief, a non-flammable, elastic, and stable QSE is reported for the first time, which is very promising in the application of the next-generation wearable devices.

1. Introduction

There is a tremendous demand for flexible batteries with the emerging applications of wearable devices, such as smartwatches, electronic textiles, roll-up displays, wearable heaters, bio-electronic devices, and soft robots [1]. While lithium-ion batteries (LIBs) are commonly used in consumer electronics and electric vehicles, they can be further improved in terms of flexibility, energy density, and safety. Among the negative electrodes, lithium metal (LM) has the lowest electrochemical potential (i.e. −3.04 V vs. the standard hydrogen electrode) and the highest theoretical specific capacity (i.e. 3860 mAh g^{-1} vs. 372 mAh g^{-1} for graphite) [2]. However, due to the uneven plating and stripping of lithium during cycling, dendrites quickly form and penetrate the separator of lithium metal batteries (LMBs), causing internal short circuits [3,4]. Furthermore, LM is highly active and reacts with the electrolyte to form a solid electrolyte interphase (SEI) [5]. The growth of lithium dendrites often cracks the SEI. Therefore, the newly exposed lithium will continue to react with the electrolyte. This phenomenon causes the material to detach from its bulk, leading to inactive or "dead" lithium [6]. As a consequence of this phenomenon, the anode utilization, cycling efficiency, and cycling life of LMBs are typically not satisfactory. Several strategies have been proposed to enhance the stability of LM, including the growth of an artificial SEI [7–15] and the use of electrolytes with a high salt concentration [16–23]. For example, flu-

Abbreviation: AEA, adiabatic electron affinity; AIBN, azobisisobutyronitrile; AIP, adiabatic ionization potential; BA, butyl acrylate; CV, cyclic voltammetry; DMC, dimethyl carbonate; DEC, diethyl carbonate; DFT, density functional theory; DSC, differential scanning calorimetry; EA, ethyl acetate; EC, ethylene carbonate; EIS, electrochemical impedance spectroscopy; EMC, ethyl methyl carbonate; EMF, EA/TMP/FEC; FEC, fluoroethylene carbonate; FTIR, fourier transform infrared spectroscopy; GCD, galvanostatic charge-discharge; HOMO, highest occupied molecular orbital; LFP, $LiFePO_4$; LIB, lithium-ion battery; LiFSI, lithium bis(fluorosulfonyl)imide; LiTFSI, lithium bis(trifluoromethylsulphonyl)imide; LM, lithium metal; LMB, lithium-metal battery; LOE, liquid organic electrolyte; LSV, linear sweep voltammetry; LUMO, lowest unoccupied molecular orbital; MF, TMP/FEC; PAN, polyacrylonitrile; PBA, poly(butyl acrylate); PC, propylene carbonate; PEO, poly(ethylene oxide); PMMA, poly(methyl methacrylate); PVDF, poly(vinylidene fluoride); QSE, quasi-solid electrolyte; RT, room temperature; SEI, solid electrolyte interphase; SEM, scanning electron microscopy; SSE, solid-state electrolyte; TBP, tributyl phosphate; TEP, triethyl phosphate; T_g, glass transition temperature; TGA, thermogravimetric analysis; TMP, trimethyl phosphate; TPP, triphenyl phosphate; XPS, X-ray photoelectron spectroscopy.

* Corresponding author.
E-mail address: mefrank@ust.hk (F. Ciucci).

https://doi.org/10.1016/j.ensm.2020.10.012
Received 3 September 2020; Received in revised form 3 October 2020; Accepted 14 October 2020
Available online 16 October 2020

oroethylene carbonate (FEC) has been adopted as a film-forming additive to generate a lithium-ion conductive and electron insulating LiF layer on the LM surface [7,24]. The LiF-containing SEI typically shows a uniform and compact morphology and leads to a significantly improved cycling stability. The Hu group [16] introduced a new class of 'solvent-in-salt' electrolytes with high concentrations (7 M) of lithium bis(trifluoromethylsulphonyl)imide (LiTFSI). Such high concentrations greatly improved the cycling life of the batteries because of the delayed dendrite formation compared to the electrolytes with low concentrations of LiTFSI (1 M). Qian et al.[17]. prepared a 4 M lithium bis(fluorosulfonyl)imide (LiFSI)/1,2-dimethoxyethane electrolyte. The resulting Li | Li symmetric cell with the electrolyte could cycle more than 6000 cycles at 10 mA cm^{-2}.

As discussed above, the unsatisfactory performance of LM causes safety concerns. Therefore, improving the safety of LMBs has become a critically important area of research. Conventional liquid organic electrolytes (LOEs), including dimethyl carbonate (DMC), diethyl carbonate (DEC), ethyl methyl carbonate (EMC), ethylene carbonate (EC), and propylene carbonate (PC), are flammable and may trigger a catastrophic failure if the heat supplied is excessive, an internal short circuit occurs, or the battery is penetrated. Incorporating flame-retarding solvents, such as trimethyl phosphate (TMP), triethyl phosphate (TEP), tributyl phosphate (TBP), and triphenyl phosphate (TPP), into the electrolyte improves the safety of the battery [25–28]. Among the various options, TMP is particularly attractive because of its high dielectric constant (ε_r=21.26), ability to dissolve lithium salts even at high concentration levels, low viscosity (2.32 mPa•s), and wide liquid temperature window (−46 – 197°C). However, TMP is unstable against LM and decomposes at a potential of 1.2 V vs. Li/Li^+ [29,30]. Moreover, using TMP does not fundamentally resolve the dendrite problem because TMP is not able to form a stable SEI on LM [30].

A fundamentally different approach to improve the safety of batteries is to employ a solid-state electrolyte (SSE). As is well known, the surface of solids, either ceramic or polymer, is not perfectly flat. The poor solid-solid contact between SSE and electrodes can lead to excessively high resistances and limit the utilization of active materials [31,32]. Replacing the SSE with a quasi-solid electrolyte (QSE) that contains a polymer skeleton and a solvent can solve this challenge. QSEs combine the advantages of solids with those of liquids, including reduced or no leakage and better contact with electrodes [33–35]. Various polymers, such as poly(ethylene oxide) (PEO), poly(vinylidene fluoride) (PVDF), polyacrylonitrile (PAN), and poly(methyl methacrylate) (PMMA) have been used to prepare QSEs [36,37]. For example, Chen et al.[38]. made a TMP-based QSE with PMMA to reinforce the non-flammable electrolyte. However, PMMA is a rigid-chain polymer material that is poorly soluble in TMP, thus hindering its application in flexible electronics and wearable devices. Furthermore, there have been no reports on non-flammable QSEs with outstanding elasticity, which is a necessary trait of high-performance wearable devices.

During the industrial production of batteries, electrodes and separators are stacked or rolled together, and the liquid electrolyte is injected to infiltrate the separators. The batteries are then sealed to complete the assembly before formation and degassing. In the case of QSE-based batteries, there are two types of preparation methods. The first one is called solution casting, which involves the dissolution of a polymer in solvents followed by casting and solvent evaporation [39]. The second method is polymerization, during which the polymer precursors, cross-linker, and initiator are mixed into a solvent and form a QSE upon heating [38,40,41] or UV treatment [42–47]. The complexity of these processes prolongs the fabrication period and increases costs. Additionally, it is challenging to control the thickness of the QSEs. The combination of these issues hinders the industrialization of QSE-based batteries. An alternative to conventional procedures is to make QSE-based batteries using in situ polymerization, the process of which is exactly the same as the traditional method except that the liquid precursor of the QSE is used instead of liquid electrolyte. Therefore, QSE-based batteries can be prepared with the conventional process and equipment in this way, making it possible to produce QSE-based batteries at large scale and low cost. Furthermore, the thickness of the QSE can be easily controlled by adjusting the separator thickness.

In this work, we developed a new non-flammable elastic QSE based on poly(butyl acrylate) (PBA) and fabricated using in situ polymerization. The incorporation of TMP allowed the QSE to be non-flammable, while FEC allowed the formation of a stable SEI on LM. Following solubility parameter theory, ethyl acetate (EA) was included to adjust the solubility of PBA in the mixed solvent. The large butyl side group of PBA provided more free volume compared with methyl. The more free volume made it easier for the polymer chains to move and, therefore, endowed the electrolyte with better flexibility and elasticity. The quasi-solid nature of the electrolyte enabled a spatially even current distribution, hampering the formation of dendrites. The LMB with $LiFePO_4$ (LFP) cathode and PBA20 electrolyte displayed a specific discharge capacity of 166 mAh g^{-1} at 0.2 C, and 153 mAh g^{-1} at 1 C, as well as stable operation at 0.5 C for 500 cycles with only a 6% of capacity decay over the whole testing period. The Li | PBA20 | Li symmetric cell showed stable stripping/plating cycling for 500 h at 0.5 mA cm^{-2} and 0.5 mAh cm^{-2}. Density functional theory (DFT) was used to analyze the mechanism of the stable cycling of the QSE-based batteries and revealed the film-forming function of FEC in forming the stable LiF-rich SEI. We also made a pouch cell with a capacity of 5.4 mAh with this method. Due to the elasticity of the electrolyte, the pouch cell could continue to function even if flexed and twisted. A ribbon-shaped battery was also prepared to show the flexibility of the electrolyte, which could operate when tied into a knot. The in situ polymerization method is compatible with the current production line of LIBs due to the low-viscosity liquid precursor, making it very easy to scale up. In this work, our battery and QSE achieved non-flammability and elasticity and provided a practical solution to the industrialization of QSE-based batteries with higher safety.

2. Experimental section

Preparation of the QSEs. The QSEs were prepared by in situ polymerization. Firstly, LiFSI was dissolved in EA/TMP/FEC (EMF) (4:3:3 by volume) mixed solvent to form a 5 M LiFSI/EMF solution. Then, the butyle acrylate (BA) monomer (20 wt.% – 50 wt.%, with 0.2 mol% of poly(ethylene glycol) dimethacrylate as cross-linker) was mixed with the solution to form the precursor solution. Azobisisobutyronitrile (AIBN) was dissolved in it as the thermal initiator. The precursor solution was injected into a glass mold with a silicone spacer. Finally, the QSE was obtained by heating the precursor at 70°C for 12 h. The obtained QSEs were denoted as PBA20 – PBA50, where the number was the weight percentage of PBA in the QSEs (20 wt.% – 50 wt.%). All of the chemicals were purchased from Sigma-Aldrich.

Materials characterizations. Scanning electron microscopy (SEM) was performed on JEOL-6390. The LMs were rinsed with DMC and naturally dried in the glove box before the SEM measurement. Fourier transform infrared spectroscopy (FTIR) was performed on Bruker ALPHA Spectrometer. X-ray photoelectron spectroscopy (XPS) was performed on an Axis Ultra DLD instrument. Differential scanning calorimetry (DSC) tests were carried out on a differential scanning calorimeter (Q1000, TA). Thermogravimetric analysis (TGA) was carried out on a thermogravimetric analyzer (Q5000, TA). The uniaxial tensile tests were conducted on a UTM-I2 universal testing machine following the ASTM D412 standard. The QSE samples were cut into the size of 50 mm × 5 mm × 1 mm and tested with a crosshead speed of 50 mm min^{-1}. At least five specimens were tested for each composition.

Electrochemical measurements. Unless specified, all electrochemical measurements were carried out in the 2032-type coin cells. LFP, super P conductive carbon, and PVDF at the weight ratio of 8:1:1 were carefully ground with mortar and pestle for 20 min. After that, N-methyl

pyrrolidone was added, and the mixture was magnetically stirred for 4 h to form a homogeneous slurry. Next, the slurry was cast on aluminum foil with a doctor blade. The slurry-coated foil was then dried in an oven at 80°C for 24 h to obtain the positive electrode. The mass loading of LFP was set at ~2 mg cm^{-2}. The LFP cathode was cut into discs with a diameter of 12 mm for further use. 2032-type coin cells were assembled in an Ar-filled glovebox (H_2O < 0.01 ppm, O_2 < 0.01 ppm, Mikrouna, China). A Celgard 2400 membrane was used as a support for the precursor solution. 50 μL of the precursor were dropped on the Celgard 2400 membrane. After the coin cells were sealed with a crimper (MSK-160D, MTI corporation, China), they were taken out of the glovebox and heated in an oven at 70°C for 12 h. Finally, the Li | QSE | LFP batteries were cooled to room temperature. A Li | QSE | LFP pouch cell was prepared by a similar method except that an aluminum-plastic film was used as the battery casing. Li | Li symmetric cells were prepared with an identical method except that LFP was replaced by a Li chip. The Li chip used in this work had a diameter of 14 mm and a thickness of 0.4 mm. A ribbon-shaped LIB with a graphite anode, an LFP cathode and heat-shrinkage tube as the battery casing was also prepared to highlight the flexibility of the electrolyte. The galvanostatic charge-discharge (GCD) tests of the batteries were carried out on a CT2001A battery testing system (Wuhan LAND Electronic Co.Ltd., China). Electrochemical impedance spectroscopy (EIS), linear sweep voltammetry (LSV) and cyclic voltammetry (CV) tests were carried out with an electrochemical workstation (VSP-300, BioLogic, France). The scan rate used for the LSV and CV tests was 5 mV/s. 2032-type coin cells with stainless steel (SS) as the working electrode and Li chip as the counter and reference electrode were analyzed by LSV and CV tests. The transference number of lithium ion (t_{Li^+}) in the electrolytes was estimated using a Li | Li symmetric cell configuration following a previously reported method [48]. A small polarization potential of 10 mV was applied to the symmetric cell, and EIS tests were carried out before and after the current reached a steady-state (2 h of relaxation time). The t_{Li^+} was obtained using

$$t_{Li^+} = \frac{I_{ss}(\Delta V - I_0 R_0)}{I_0(\Delta V - I_{ss} R_{ss})} \quad (1)$$

where ΔV is the polarization potential, I_0 is the initial current, I_{ss} is the steady-state current, and R_0 and R_{ss} are the initial and steady-state charge transfer resistances, respectively.

DFT calculations

All DFT calculations were carried in Gaussian 09 with a hybrid B3LYP functional [49] and 6–31++G(d,p) basis set [50]. The molecular structures of different electrolyte components were first optimized. Next, the energy of molecular orbitals was obtained using the optimal molecular structures. The highest occupied molecular orbital (HOMO) and lowest unoccupied molecular orbital (LUMO) were visualized with GaussView 5.0.9 [51].

3. Results and discussion

3.1. Physical and chemical properties of the electrolytes

When phosphorus-containing chemicals are heated, a polymeric form of phosphoric acid is formed, leading to a char layer, which shields the material from oxygen [52]. Phosphates, such as TMP, TEP, TBP, and TPP, have been incorporated into liquid electrolytes to make them non-flammable [25,26]. In this work, by incorporating TMP into the QSE precursors, we obtained non-flammable QSEs after in situ polymerization. The schematics in Fig. 1 outline the experimental process. We chose BA as the monomer because the butyl side group is relatively large compared with methyl. Its larger volume reduced the intermolecular interaction between PBA polymer chains. Moreover, larger side groups provided more free volume for PBA and improved the ability of the polymer to trap the solvent molecules. The glass transition temperature (T_g) of PBA and PMMA were measured with DSC, as shown in Fig. 2b-c. From the DSC curves, we estimated the T_g of PBA to be −23°C, a value significantly lower than that of PMMA (105°C) [53]. According to free volume theory [54], the free volume ratio of a polymer depends inversely on T_g. The DSC results of PBA and PMMA indicate that the larger volume of the butyl group compared to the methyl group endows PBA with lower T_g than PMMA. This result is consistent with the theory [54]. The difference of T_g indicates that PBA is rubber at room temperature (RT) while PMMA is a plastic material. We could also observe that PBA without cross-linking could flow at RT, while PMMA is rigid and brittle, behaving as an “organic glass” (Figure S1).

Following solubility parameter theory, the closer the solubility parameter, δ, of the polymer to that of the solvent, the better will be the solubility of the polymer in the solvent [55]. In detail, we can write

$$\delta_k = \frac{\rho}{M} \sum G \quad (2)$$

where M is the molar mass of the molecule, ρ is the density, and ΣG is the sum of the molar attraction constants of all groups making up the molecule [56]. The solubility of the mixed solvent can then be calculated as

$$\delta_M = \sum_i \delta_i \varphi_i \quad (3)$$

where δ_M is the solubility parameter of the mixed solvent and φ_i is the volume fraction of the ith component. The solubility parameters for each solvent, as well as the polymer, are listed in Table S1. The solubility parameters of TMP and FEC were calculated using (2) as 19.95 $MPa^{1/2}$ and 19.47 $MPa^{1/2}$, two values significantly higher than that of PBA (18.80 $MPa^{1/2}$), indicating that they are poor solvents for PBA. In order to dissolve PBA, we incorporated EA into the solvent. The resulting EMF solvent had a solubility parameter of 19.08 $MPa^{1/2}$. The latter value is closer to that of PBA, implying that PBA has good solubility in EMF. Figure S3 shows that without the addition of EA, the TMP/FEC (MF) mixed solvent could not dissolve PBA very well, and phase separation occurred after polymerization. In contrast, the PBA/EMF mixture was uniform, indicating PBA’s excellent solubility in EMF. As is known, the solvent in QSEs based on a polymer skeleton serves as plasticizer [57–59]. Further, the solvent molecules are trapped by the polymer network. Better solubility of the polymer in the solvent produces a stronger interaction between the two. Therefore, the QSE can accommodate more solvent, compared to the case where the polymer is poorly soluble in the solvent. It should be noted that we also included 0.2 mol% of poly(ethylene glycol) dimethacrylate as the cross-linker to stabilize the polymer skeleton. The lower content of the cross-linker was not sufficient to keep the skeleton stable, while higher amounts made the electrolyte brittle. SEM was used to characterize the morphology of the polymerized QSE supported by Celgard separator (see Figure S4). The SEM images show smooth and compact morphology, which is beneficial for the uniform deposition of Li.

FTIR was used to verify the polymerization of BA, see Fig. 2a. The BA monomer showed intense absorption peaks at 1628 cm^{-1}, 974 cm^{-1}, and 810 cm^{-1}, corresponding to the C=C stretch, $=CH_2$ wag, and =CH wag [60–62]. After polymerization, however, these peaks almost disappeared, as can be seen in the spectrum of PBA, indicating the successful completion of the polymerization process. We also found that the carbonyl group of BA appeared at lower wavenumber (1721 cm^{-1}) than that of PBA (1728 cm^{-1}) because of the hybridization of the C=C–C=O bonds, which lowered the electron cloud density around C=O [63]. This phenomenon further confirmed the conversion from BA to PBA. FTIR tests of the PBA/EMF QSE, BA/EMF precursor, and individual electrolyte components were also carried out (see Figure S5). The absorption peak of CH_2–CH in BA at 1628 cm^{-1} was detected for the BA/EMF precursor (before polymerization). The other two peaks at 974 cm^{-1} and 810 cm^{-1} were indistinguishable because they overlapped with those of other electrolyte components. However, these three peaks disappeared

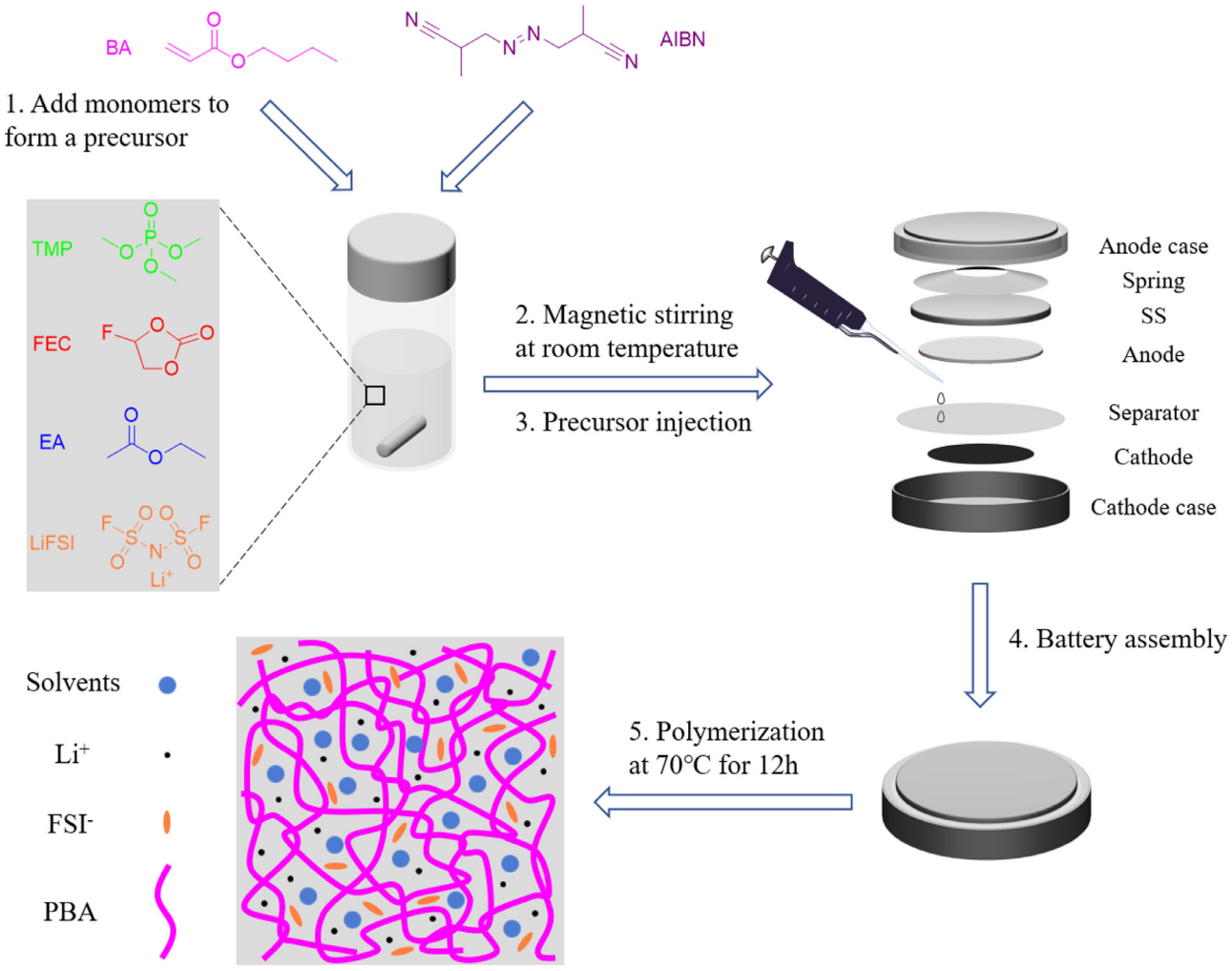

Fig. 1. Schematic of the battery assembly. The precursor solution was dropped on the Celgard separator support. The battery was then sealed and heated to allow the polymerization.

in PBA/EMF QSE after polymerization, indicating BA's complete conversion into PBA.

Fig. 2d shows the typical stress-strain curves of the QSEs for various PBA concentrations. The tensile properties, including tensile strength, Young's modulus, strain at break, and toughness of the PBA-based electrolytes, are displayed in Fig. 2e. When PBA content increased from 30 wt.% to 50 wt.%, the tensile strength increased monotonically from 66.38 ± 2.69 kPa to 100.14 ± 10.20 kPa, reflecting the reinforcing effect of the polymer. Interestingly, the tensile strength of PBA20 was higher than that of PBA30 and PBA40 and close to that of PBA50. Such a higher strength can be attributed to the higher mobility of the polymer chain segments in PBA20 because of the higher solvent content (80 wt.%). The molecular chains can easily align under load so that the stress is distributed evenly along these chains, allowing a higher total stress before failure. The same mechanism is also reflected in an increased slope of the stress-strain curve of PBA20 in the range of 500% – 600% of strain in Fig. 2d. The Young's moduli of the electrolytes, which were calculated according to the initial slopes of the stress-strain curves, also increased monotonically from 40.00 ± 11.77 kPa to 95.14 ± 7.30 kPa with increasing PBA content, see Fig. 2e. Notably, the strain at break of PBA20 reached 646%, indicating the outstanding elasticity of the PBA-based electrolyte. As mentioned above, the large butyl group provided more free volume for the chain segments to relax. Therefore, the molecular chain of the polymer could be stretched along the direction of the load. Thanks to this property, the toughness of the PBA-based electrolytes, calculated by integrating the area under the stress-strain curves of tensile tests, also improved [64–66]. The toughness of PBA20 was as high as 219.41 ± 30.97 kJ m^{-3}. Such a high toughness value makes the electrolyte a promising candidate for flexible batteries. Video S1 demonstrates the stretchability of the QSE.

3.2. Electrochemical performances

The conductivities of the electrolytes with various PBA contents in the range of 0°C to 90°C were measured by clamping the electrolytes between two SS plates. As shown in Fig. 3a-b, the electrolyte conductivity decreases with increasing PBA content. This trend can be understood using Physico-chemical intuition. Within the electrolyte, PBA serves as a physical skeleton that confines the solvent molecules. Concomitantly, the solvents not only act as the plasticizers but also dissolve and dissociate the Li salt and promote the movement of the polymer chains. The last two traits greatly benefit the transportation of Li^+. Therefore, the conductivities increase with increasing solvent concentration. As a result, PBA20 has the highest ionic conductivity (3.3×10^{-4} S cm^{-1} at 30°C vs. 1.23×10^{-3} S cm^{-1} at 30°C of the LOE, i.e., 1 M $LiPF_6$ in EC:DEC:EMC=1:1:1 vol.%) among the materials studied. The conductivity follows the Arrhenius equation:

$$\sigma(T) = \sigma_0 e^{-E_a/k_B T} \quad (4)$$

where $\sigma(T)$ is the conductivity at temperature T, σ_0 is the preexponential factor, E_a is the activation energy, and k_B is the Boltzmann constant.

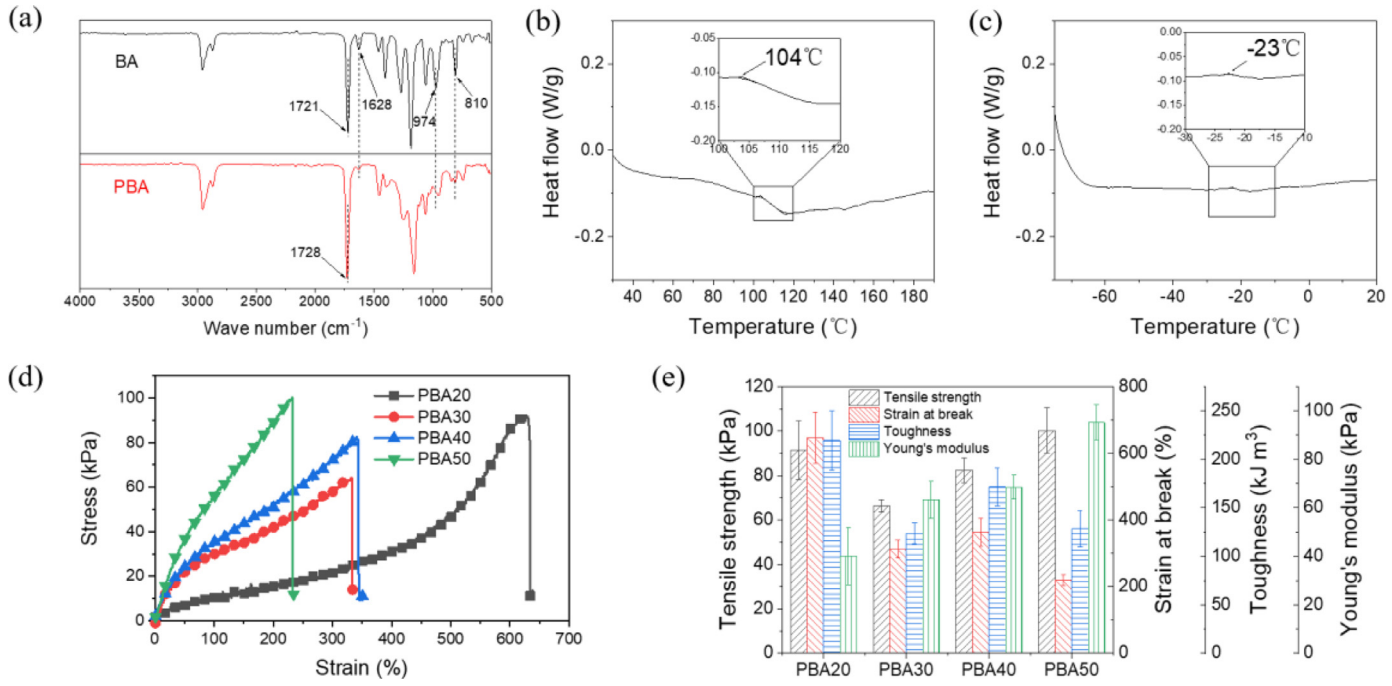

Fig. 2. (a) FITR spectra of BA and PBA. DSC curves of (b) PMMA and (c) PBA. (d) Stress-strain curves of PBA-based electrolytes with different polymer contents and (e) corresponding mechanical properties.

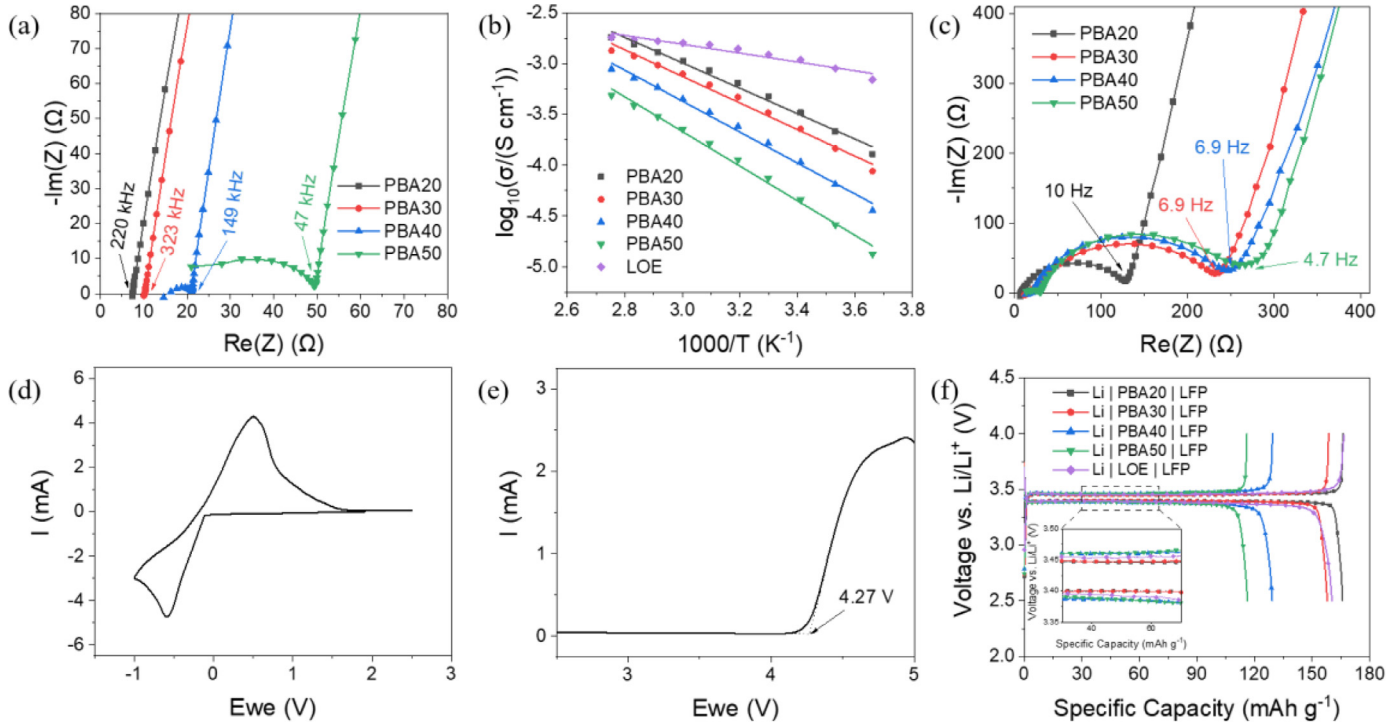

Fig. 3. Electrochemical properties of the PBA-based QSEs. (a) EIS curves of PBA-based QSEs with various PBA contents clamped between stainless steel spacers. (b) Conductivities of the electrolytes as a function of temperature. (c) Nyquist plots of the EIS of fully discharged Li | PBA | LFP LMBs. (d) CV and (e) LSV curves of the PBA20 electrolyte with SS as working electrode and Li chip as the counter and reference electrode. (f) Charge-discharge profiles of the LMBs with QSEs.

At 0°C, the conductivity of PBA20 was 1.3×10^{-4} S cm^{-1}. When the temperature was increased to 90°C, the conductivity was measured to be 1.8×10^{-3} S cm^{-1}. The E_a of a conventional liquid electrolyte is only 0.09 eV, while the E_a of PBA20 is 0.25 eV, a significantly higher value. The higher PBA content in the QSE leads to higher E_a (Table 1). The reason for this is that the movement of polymer chains requires considerably higher energy than small-molecule solvents. Therefore, the conductivity is more sensitive to temperature. The CV curve in Fig. 3d shows the reversible plating and stripping of Li on the anode, as indicated by the anodic peak at −0.59 V and the cathodic peak at 0.50 V, respectively. Fig. 3e shows the LSV curve of the QSE, indicating that the QSE was electrochemically stable below 4.27 V. The current drastically

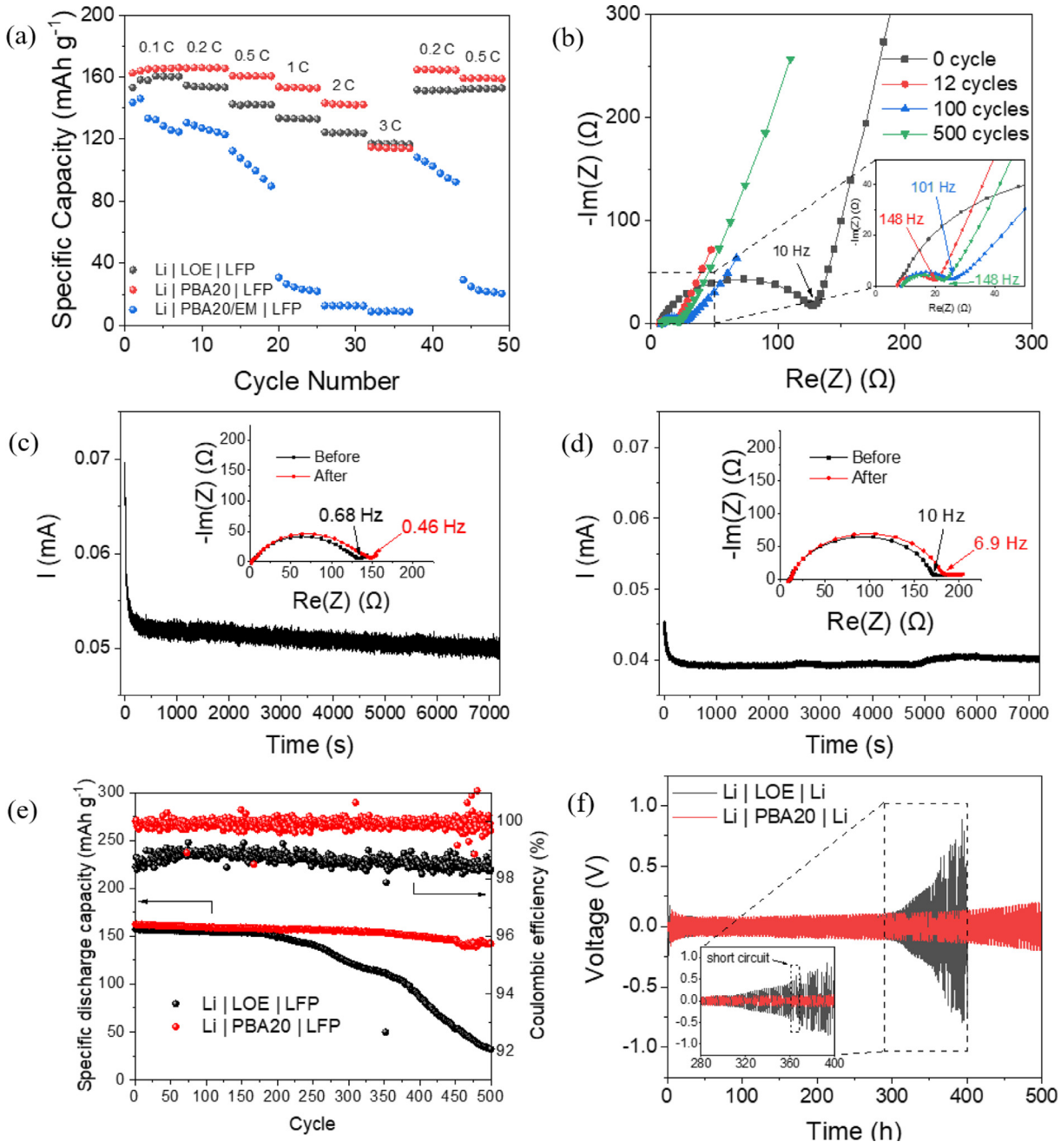

Fig. 4. Electrochemical performance of the LMs. (a) Rate capabilities of the LMBs with LFP as the cathode and LOE, PBA20, and PBA20/EM as the electrolyte. (b) EIS curves of Li | PBA20 | LFP battery after different cycles. t_{Li^+} of the symmetric cells with (c) conventional LOE and (d) QSE. Long-term cycling stability of the (e) LMBs and (f) symmetric cells with LOE and QSE.

increased at higher voltages, likely because of the decomposition of the polypropylene support as suggested in the literature [67–69].

The electrochemical performance of the PBA-based QSEs was evaluated using 2032-type LMBs. EIS tests were carried out to get the R_{ct} (see Fig. 3c), and the curves were fitted with an equivalent circuit (Figure S7 and Table S2). The LMB with PBA20 QSE had the lowest charge transfer resistance (126.3 Ω). As shown in Fig. 4a and Figure S8, the Li | PBA20 | LFP LMB delivered a high capacity of 166 mAh g^{-1} at 0.1 C, approaching the theoretical capacity of LFP (170 mAh g^{-1}). The capacity was 166 mAh g^{-1} at 0.2 C, 161 mAh g^{-1} at 0.5 C, and 153 mAh g^{-1} at 1 C, see Fig. 4a. Even at a high rate of 3 C, a capacity of 114 mAh g^{-1} was retained. When the current density went back to 0.5 C, the capacity remained 159 mAh g^{-1}. The excellent rate capability was a result of the electrolyte's high ionic conductivity and small thickness (25 μm, equal to that of the Celgard support). This is also evidenced by the charge-discharge profiles in Figure S9. The overpotential of the Li | PBA20 | LFP is only 46 mV at 0.1 C, and 154 mV at 1 C, in agreement with the low bulk resistance of about 7.4 Ω observed in EIS graphs. This value was even lower than the overpotential measured for the conventional LOE, 65 mV at 0.1 C, see Fig. 3f. The low overpotential is likely due to the in situ polymerization that lowers the R_{ct} [70].

The low overpotential of the QSE-based LMBs could also be due to the high lithium ion transference number (t_{Li^+}). As anions migrate toward a different electrode compared with Li ions (i.e., toward the cathode/anode when the battery is charging/discharging), a concentration gradient builds up. In turn, such a gradient slows the migration of Li

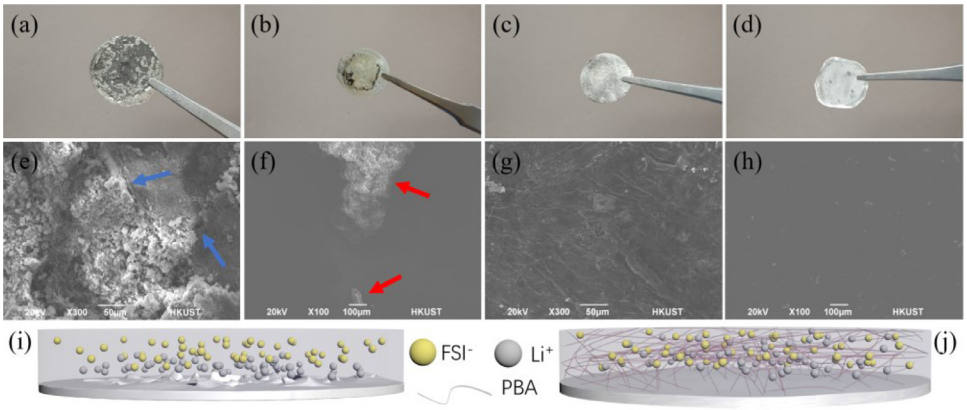

Fig. 5. Optical and SEM images of the LMs and separators cycled with LOE (a, b, e, f) and QSEs (c, d, g, h).

ions and increases the overpotential. To verify the impact of t_{Li^+}, we measured the t_{Li^+} of the symmetric cells with conventional LOE and QSE, see Fig. 4c-d. The result shows that the t_{Li^+} in LOE was only 0.24, while it reached 0.63 in the QSE, suggesting that concentration gradient effects are reduced. The high t_{Li^+} of the QSE could be attributed to two factors: 1) the polymer skeleton could limit the movement of anions; [71] 2) the Li^+ cations were less solvated with high salt concentration compared to low salt concentration, leading to higher Li^+ mobility [16].

Interestingly, the specific capacities of the QSE-based batteries increased during the first a few cycles. The same phenomenon has been observed in other systems, including gel-like electrolytes [72–75]. We conjecture that such an increase is due to the fact that interfacial resistance between electrode and electrolyte decreased upon cycling. To investigate this hypothesis, we carried out EIS tests of the LMB after different cycles, and compared them with the newly prepared battery before cycling, as shown in Fig. 4b. The R_{ct} was reduced significantly after 12 cycles of operation and was virtually unchanged after that. These results can be easily rationalized by noting that the molecular chains move slowly during the cycling, enabling better contact between the electrolyte and the electrode, thus allowing better utilization of cathode material.

Long-term cycling stability of the QSE-based LMBs was also characterized by GCD (results displayed in Fig. 4e-f). As a reference, the LMB with conventional LOE showed a stable capacity within the first 170 cycles and started to decay after that. After 500 cycles, only 20% of the capacity was retained, along with an average coulombic efficiency of 98.7%. In contrast, the QSE-based LMBs were able to remain stable cycling for 500 cycles, with 94% of capacity retention and an average coulombic efficiency higher than 99.9%. The capacity decay of PBA-based QSE-based LMB was only 0.012% per cycle. Our work showed outstanding cycling performance compared to recent studies on QSE-based LMBs (see Table S3). Li | Li symmetric cells were also prepared to assess the cycling stability of LM in different electrolytes, as shown in Fig. 6f. A short circuit occurred after 238 h of plating and stripping when LOE was adopted, while stable cycling for more than 500 h was achieved for QSE.

The electrochemical results imply that the LOE continuously reacted with the electrolyte, causing a low coulombic efficiency and a decreased discharge capacity. The continuous reaction led to an uneven deposition of lithium on LM damaging the SEI and to the exposure of "fresh" lithium that continuously reacted with the electrolyte. The polymer skeleton of the QSE facilitated the uniform plating and stripping of lithium as illustrated in the schematics of Fig. 5i-j [76–78]. To verify that, we observed the morphologies of the LMs and separators both optically and by SEM, see Fig. 5. The LM surface with the LOE showed dark deposition spots, which were also found on the separator. In addition, the separator was dry, implying that the LOE was consumed by the continuous reaction with LM. The SEM further allowed us to observe that dark spots were

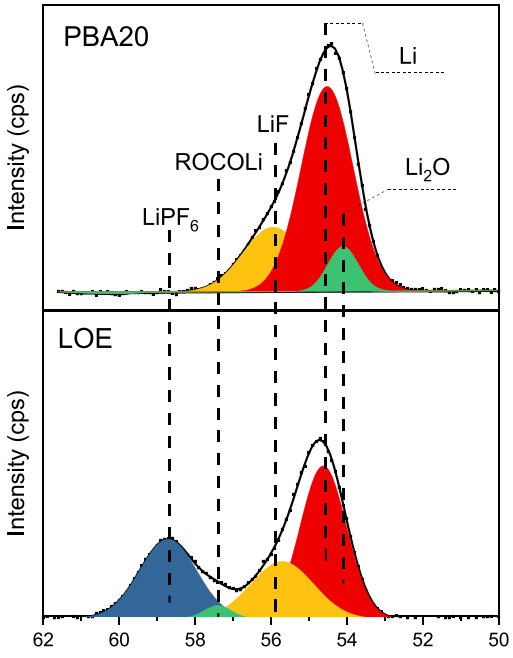

Fig. 6. XPS Li 1 s spectra of the LMs cycled in LOE and PBA20 electrolytes.

porous and unevenly distributed, likely a mixture of reaction products and dead lithium. In contrast, the surface of LM cycled with the QSE was clean and free of black spots, and no deposition was found on the separator. SEM showed a clean and dense LM surface, suggesting that the plating and stripping of Li occurrend uniformly for the battery with the QSE.

XPS was carried out to characterize the LMs cycled in LOE and PBA20 electrolytes as shown in Fig. 6. As can be seen, LiF formed on the LM after cycling in PBA20 QSE. Combined with the SEM result above, we observed that the LiF-rich SEI created by FEC was compact and robust. The SEI formed in LOE also contained LiF due to the decomposition of $LiPF_6$. However, it was very porous and could not prevent the continuous reaction between the LM and the carbonate-based electrolyte. Moreover, organic component ROCOLi was also found in the SEI as a result of the decomposition of carbonates, which contributed to the porous morphology of the LM surface [79].

3.3. DFT calculations

In order to probe the mechanism of stable cycling for QSEs, we used DFT to analyze the components of QSE and LOE. The HOMO and LUMO of EA, TMP, FEC, FSI^-, and PBA unit were calculated, as shown in Fig. 7a

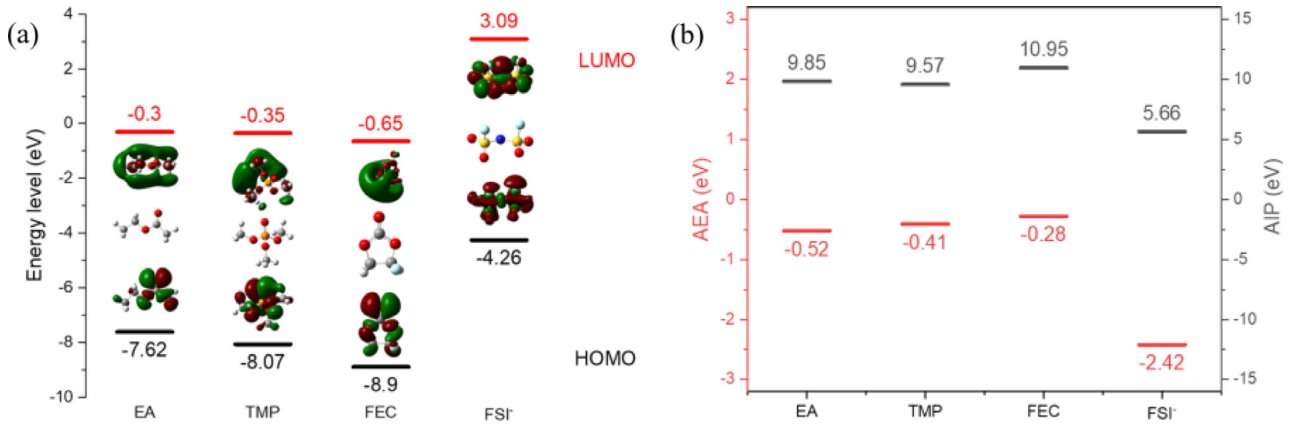

Fig. 7. DFT calculations of (a) the HOMO, LUMO, (b) AEA, and AIP of different QSE components.

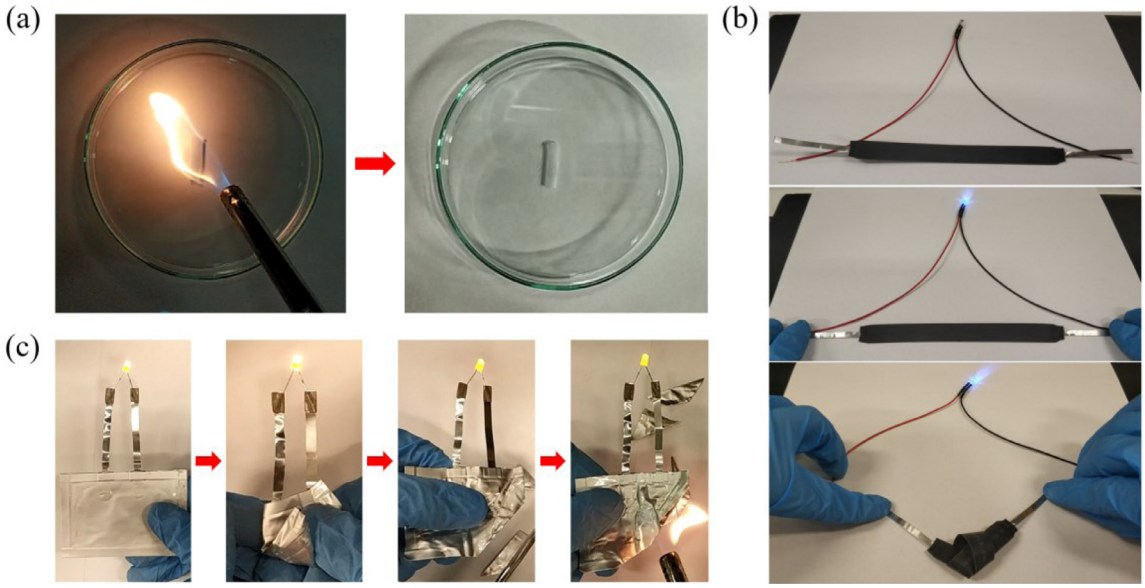

Fig. 8. Demonstration of non-flammable and flexible batteries based on QSE. (a) Flammability test of the QSE. (b) Ribbon-shaped QSE-based battery could light an LED light when tied into a knot. (c) The QSE-based pouch cell continued to work when folded, cut out and exposed to fire.

Table 1
Bulk resistance, thickness, conductivity, and activation energy of different electrolytes at room temperature.

	R_b (Ω)	Thickness (μm)	Conductivity (S cm^{-1})	E_a (eV)
PBA20	7.4	25	4.2×10^{-4}	0.25
PBA30	10.1	25	3.1×10^{-4}	0.26
PBA40	21.0	25	1.5×10^{-4}	0.30
PBA50	49.4	25	6.3×10^{-5}	0.34
LOE	2.68	25	1.2×10^{-3}	0.09

Table 2
HOMO, LUMO, AEA, and AIP of different electrolyte components.

	HOMO (eV)	LUMO (eV)	AEA (eV)	AIP (eV)
EA	−7.62	−0.30	−0.52	+9.85
TMP	−8.07	−0.35	−0.41	+9.57
FEC	−8.90	−0.65	−0.28	+10.95
FSI^-	−4.26	+3.09	−2.42	+5.66
H-BA-H	−7.59	−0.30	−0.44	+9.52
EC	−8.39	−0.61	−0.29	+10.55
DEC	−4.26	3.09	−2.42	+5.66
EMC	−8.08	−0.25	−0.51	+10.22
$PF6^-$	−5.40	+4.07	−5.17	7.90

and Table 2. FEC was computed to have the lowest LUMO among all studied compounds. This result implies that FEC is the most susceptible to reduction at the anode [80–82]. The reduction of FEC leads to the formation a LiF-rich SEI which is Li^+-conducting and electron-insulating layer [7,24,83–85]. Therefore, using FEC prevents the reaction between TMP and LM. In turn, this leads to the stable cycling of the QSE-based LMBs.

To further prove the effect of FEC, we calculated the adiabatic electron affinity (AEA) and adiabatic ionization potential (AIP) of the different electrolyte components, see Fig. 7b. AEA and AIP are defined as follows: [86]

$$AEA = E_M - E_{M^-} \quad (5)$$

$$AIP = E_{M^+} - E_M \quad (6)$$

where E_M, E_{M^-} and E_{M^+} are the energies of a component and the corresponding anion and cation, respectively.The higher the AEA, the more capable a compound is to be reduced [86]. FEC has the highest AEA among all the components, corresponding to the highest tendency to be reduced by LM, which is consistent with the frontier orbital analysis result.

We also calculated the HOMO, LUMO, AEA, and AIP of the LOE components, with the results listed in Table 2. Due to the highest LUMO and lowest AEA of PF_6^-, LiF was formed after the decomposition of EC, DEC and EMC. Therefore, instead of forming a compact LiF-rich SEI layer, the surface of the LM after cycling in LOE was porous. It has been reported that the decomposition of carbonates, such as EC and DMC, leads to the segregation of LiF in the organic matrix to form an inhomogeneous and porous SEI [79,87], which is consistent with our SEM and DFT results.

3.4. Non-flammable and flexible batteries

To demostrate the high safety of the QSE, we carried out a qualitative flammability test by exposing the electrolyte to the flame originating from a lighter with butane as fuel. The electrolyte was not ignited (Fig. 8a and Video S2), demonstrating its non-flammability and high safety. In contrast, the conventional LOE caught fire immediately (Figure S10 and Video S3).

To demonstrate the feasibility of making flexible batteries with the PBA20-based QSE, we prepared the pouch cell and ribbon-shaped batteries shown in Fig. 8. The in situ polymerization method is compatible with the current industrial production techniques because the liquid precursor can be easily infiltrated into the separator, which allowed us to scale up and make batteries of different shapes following the processes typical of LIB production. As shown in Fig. 8b, the ribbon-shaped battery can power an LED light even when tied into a knot. The pouch cell, which had a capacity of 5.4 mAh, can work if folded, cut out, and exposed to a flame (Fig. 8c), proving its outstanding flexibility and safety. In contrast, pouch cells with LOE and PBA20/MF as electrolyte stopped working when they were bent (see Figure S11, Video S5 and Video S6), demonstrating the significance of designing elastic polymer electrolyte.

4. Conclusions

We developed a new QSE with high elasticity and non-flammability. The electrolyte showed excellent stretchability, with a strain at break higher than 600% when 20 wt.% of PBA was incorporated. The conductivity of PBA20 electrolyte reached 4.2×10^{-4} S cm^{-1} at 23°C, and the overpotential of the Li | PBA20 | LFP LMB was as low as 46 mV at 0.1 C as a result of the good interfacial contact with the electrodes brought by the in situ polymerization method. Thanks to the high concentration Li salt and the addition of FEC, the QSE-based LMB cycled stably 500 times at 0.5 C with a final 94% capacity retention. The mechanism of the stable cycling was demonstrated by DFT calculation, which proves the significance of FEC in forming the SEI protecting layer on the anode, enabling the reversible plating and stripping of Li for more than 500 h. A ribbon-shaped battery and a pouch cell were also prepared to prove the feasibility of making flexible batteries with our QSE. The PBA-based electrolyte achieved non-flammability and elasticity simultaneously, which shows potential for the next-generation wearable devices in the future.

Declaration of Competing Interest

The authors declare that they have no known competing financial interests or personal relationships that could have appeared to influence the work reported in this paper.

CRediT authorship contribution statement

Guodong Zhou: Conceptualization, Data curation, Formal analysis, Funding acquisition, Methodology, Software, Visualization, Writing - original draft. **Xidong Lin:** Conceptualization, Methodology. **Jiapeng Liu:** Software, Visualization. **Jing Yu:** Methodology. **Junxiong Wu:** Methodology. **Ho Mei Law:** Methodology. **Zheng Wang:** Software. **Francesco Ciucci:** Resources, Writing - review & editing, Supervision, Project administration, Funding acquisition.

Acknowledgments

The authors acknowledge the support from the Research Grants Council of Hong Kong (projects 16227016, and 16204517), the Hong Kong Innovation and Technology Fund (ITS/292/18FP), and the Guangzhou Science and Technology Program (no. 201807010074). The authors thank Dr. Mingxu Cui for the help with FTIR characterization. The authors also appreciate the technical assistance from the Advanced Engineering Materials facilities (AEMF) and the Materials Characterization and Preparation Facilities (MCPF) of HKUST.

Supplementary materials

Supplementary material associated with this article can be found, in the online version, at doi:10.1016/j.ensm.2020.10.012.

References

[1] J. Chang, Q. Huang, Z. Zheng, A Figure of Merit for Flexible Batteries, Joule 4 (2020) 1346–1349.
[2] D. Lin, Y. Liu, Y. Cui, Reviving the lithium metal anode for high-energy batteries, Nat. Nanotechnol. 12 (2017) 194–206.
[3] W. Xu, J. Wang, F. Ding, X. Chen, E. Nasybulin, Y. Zhang, J.-G. Zhang, Lithium metal anodes for rechargeable batteries, Energy Environ. Sci. 7 (2014) 513–537.
[4] X.-B. Cheng, R. Zhang, C.-Z. Zhao, Q. Zhang, Toward safe lithium metal anode in rechargeable batteries: a review, Chem. Rev. 117 (2017) 10403–10473.
[5] K. Xu, Nonaqueous Liquid Electrolytes for Lithium-Based Rechargeable Batteries, Chem. Rev. 104 (2004) 4303–4418.
[6] K.-H. Chen, K.N. Wood, E. Kazyak, W.S. LePage, A.L. Davis, A.J. Sanchez, N.P. Dasgupta, Dead lithium: mass transport effects on voltage, capacity, and failure of lithium metal anodes, J. Mater. Chem. A 5 (2017) 11671–11681.
[7] R. Mogi, M. Inaba, S.-K. Jeong, Y. Iriyama, T. Abe, Z. Ogumi, Effects of some organic additives on lithium deposition in propylene carbonate, J. Electrochem. Soc. 149 (2002) A1578–A1583.
[8] G.A. Umeda, E. Menke, M. Richard, K.L. Stamm, F. Wudl, B. Dunn, Protection of lithium metal surfaces using tetraethoxysilane, J. Mater. Chem. 21 (2011) 1593–1599.
[9] F. Marchioni, K. Star, E. Menke, T. Buffeteau, L. Servant, B. Dunn, F. Wudl, Protection of lithium metal surfaces using chlorosilanes, Langmuir 23 (2007) 11597–11602.
[10] R.S. Thompson, D.J. Schroeder, C.M. López, S. Neuhold, J.T. Vaughey, Stabilization of lithium metal anodes using silane-based coatings, Electrochem. Commun. 13 (2011) 1369–1372.
[11] N.-S. Choi, Y.M. Lee, J.H. Park, J.-K. Park, Interfacial enhancement between lithium electrode and polymer electrolytes, J. Power Sour. 119-121 (2003) 610–616.
[12] N.-S. Choi, Y.M. Lee, K.Y. Cho, D.-H. Ko, J.-K. Park, Protective layer with oligo(ethylene glycol) borate anion receptor for lithium metal electrode stabilization, Electrochem. Commun. 6 (2004) 1238–1242.
[13] N.-S. Choi, Y.M. Lee, W. Seol, J.A. Lee, J.-K. Park, Protective coating of lithium metal electrode for interfacial enhancement with gel polymer electrolyte, Solid State Ion. 172 (2004) 19–24.
[14] D.G. Belov, O.V. Yarmolenko, A. Peng, O.N. Efimov, Lithium surface protection by polyacetylene in situ polymerization, Synth. Met. 156 (2006) 745–751.
[15] M. Wu, Z. Wen, Y. Liu, X. Wang, L. Huang, Electrochemical behaviors of a Li3N modified Li metal electrode in secondary lithium batteries, J. Power Sour. 196 (2011) 8091–8097.
[16] L. Suo, Y.-S. Hu, H. Li, M. Armand, L. Chen, A new class of Solvent-in-Salt electrolyte for high-energy rechargeable metallic lithium batteries, Nat. Commun. 4 (2013) 1481.
[17] J. Qian, W.A. Henderson, W. Xu, P. Bhattacharya, M. Engelhard, O. Borodin, J.-G. Zhang, High rate and stable cycling of lithium metal anode, Nat. Commun. 6 (2015) 6362.
[18] S.-K. Jeong, H.-Y. Seo, D.-H. Kim, H.-K. Han, J.-G. Kim, Y.B. Lee, Y. Iriyama, T. Abe, Z. Ogumi, Suppression of dendritic lithium formation by using concentrated electrolyte solutions, Electrochem. Commun. 10 (2008) 635–638.
[19] J. Qian, B.D. Adams, J. Zheng, W. Xu, W.A. Henderson, J. Wang, M.E. Bowden, S. Xu, J. Hu, J.-G. Zhang, Anode-Free Rechargeable Lithium Metal Batteries, Adv. Funct. Mater. 26 (2016) 7094–7102.
[20] K. Yoshida, M. Nakamura, Y. Kazue, N. Tachikawa, S. Tsuzuki, S. Seki, K. Dokko, M. Watanabe, Oxidative-stability enhancement and charge transport mechanism in glyme–lithium salt equimolar complexes, J. Am. Chem. Soc. 133 (2011) 13121–13129.
[21] K. Matsumoto, K. Inoue, K. Nakahara, R. Yuge, T. Noguchi, K. Utsugi, Suppression of aluminum corrosion by using high concentration LiTFSI electrolyte, J. Power Sour. 231 (2013) 234–238.

[22] Y. Yamada, M. Yaegashi, T. Abe, A. Yamada, A superconcentrated ether electrolyte for fast-charging Li-ion batteries, Chem. Commun. 49 (2013) 11194–11196.
[23] Y. Yamada, K. Furukawa, K. Sodeyama, K. Kikuchi, M. Yaegashi, Y. Tateyama, A. Yamada, Unusual stability of acetonitrile-based superconcentrated electrolytes for fast-charging lithium-ion batteries, J. Am. Chem. Soc. 136 (2014) 5039–5046.
[24] X.-.Q. Zhang, X.-.B. Cheng, X. Chen, C. Yan, Q. Zhang, Fluoroethylene carbonate additives to render uniform Li deposits in lithium metal batteries, Adv. Funct. Mater. 27 (2017) 1605989.
[25] X. Wang, C. Yamada, H. Naito, G. Segami, K. Kibe, High-concentration trimethyl phosphate-based nonflammable electrolytes with improved charge–discharge performance of a graphite anode for lithium-ion cells, J. Electrochem. Soc. 153 (2005) A135.
[26] J. Wu, J. Liu, Z. Lu, K. Lin, Y.-.Q. Lyu, B. Li, F. Ciucci, J.-.K. Kim, Non-flammable electrolyte for dendrite-free sodium-sulfur battery, Energy Storage Mater. (2019).
[27] S. Takeuchi, S. Yano, T. Fukutsuka, K. Miyazaki, T. Abe, Electrochemical intercalation/de-intercalation of lithium ions at graphite negative electrode in TMP-based electrolyte solution, J. Electrochem. Soc. 159 (2012) A2089–A2091.
[28] Q. Wang, B. Mao, S.I. Stoliarov, J. Sun, A review of lithium ion battery failure mechanisms and fire prevention strategies, Prog. Energy Combust. Sci. 73 (2019) 95–131.
[29] X. Wang, E. Yasukawa, S. Kasuya, Nonflammable trimethyl phosphate solvent-containing electrolytes for Lithium-ion batteries: I. Fundamental properties, J. Electrochem. Soc. 148 (2001) A1058.
[30] X. Wang, E. Yasukawa, S. Kasuya, Nonflammable trimethyl phosphate solvent-containing electrolytes for Lithium-ion batteries: II. The use of an amorphous carbon anode, J. Electrochem. Soc. 148 (2001) A1066.
[31] K. Fu, Y. Gong, B. Liu, Y. Zhu, S. Xu, Y. Yao, W. Luo, C. Wang, S.D. Lacey, J. Dai, Y. Chen, Y. Mo, E. Wachsman, L. Hu, Toward garnet electrolyte–based Li metal batteries: an ultrathin, highly effective, artificial solid-state electrolyte/metallic Li interface, Sci. Adv. 3 (2017) e1601659.
[32] Q. Zhao, X. Liu, S. Stalin, K. Khan, L.A. Archer, Solid-state polymer electrolytes with in-built fast interfacial transport for secondary lithium batteries, Nature Energy 4 (2019) 365–373.
[33] A. Arya, A.L. Sharma, Polymer electrolytes for lithium ion batteries: a critical study, Ionics 23 (2017) 497–540.
[34] Z. Xue, D. He, X. Xie, Poly(ethylene oxide)-based electrolytes for lithium-ion batteries, J. Mater. Chem. A 3 (2015) 19218–19253.
[35] M. Marcinek, J. Syzdek, M. Marczewski, M. Piszcz, L. Niedzicki, M. Kalita, A. Plewa-Marczewska, A. Bitner, P. Wieczorek, T. Trzeciak, M. Kasprzyk, P. Łężak, Z. Zukowska, A. Zalewska, W. Wieczorek, Electrolytes for Li-ion transport – Review, Solid State Ion. 276 (2015) 107–126.
[36] F. Baskoro, H.Q. Wong, H.-.J. Yen, Strategic structural design of a gel polymer electrolyte toward a high efficiency Lithium-ion battery, ACS Appl. Energy Mater. 2 (2019) 3937–3971.
[37] L. Long, S. Wang, M. Xiao, Y. Meng, Polymer electrolytes for lithium polymer batteries, J. Mater. Chem. A 4 (2016) 10038–10069.
[38] J. Chen, Z. Yang, G. Liu, C. Li, J. Yi, M. Fan, H. Tan, Z. Lu, C. Yang, Reinforcing concentrated phosphate electrolytes with in-situ polymerized skeletons for robust quasi-solid lithium metal batteries, Energy Storage Mater. 25 (2020) 305–312.
[39] M. Zhu, J. Wu, Y. Wang, M. Song, L. Long, S.H. Siyal, X. Yang, G. Sui, Recent advances in gel polymer electrolyte for high-performance lithium batteries, J. Energy Chem. 37 (2019) 126–142.
[40] D. Zhou, Y.B. He, R.L. Liu, M. Liu, H.D. Du, B.H. Li, Q. Cai, Q.H. Yang, F.Y. Kang, In situ synthesis of a hierarchical all-solid-state electrolyte based on nitrile materials for high-performance Lithium-ion batteries, Adv. Energy Mater. 5 (2015) 1500353.
[41] X. Xu, K. Lin, D. Zhou, Q. Liu, X. Qin, S. Wang, S. He, F. Kang, B. Li, G. Wang, Quasi-solid-state dual-ion sodium metal batteries for low-cost energy storage, Chem 6 (2020) 902–918.
[42] M.-.K. Song, J.-.Y. Cho, B.W. Cho, H.-.W. Rhee, Characterization of UV-cured gel polymer electrolytes for rechargeable lithium batteries, J. Power Sour. 110 (2002) 209–215.
[43] B. Rupp, M. Schmuck, A. Balducci, M. Winter, W. Kern, Polymer electrolyte for lithium batteries based on photochemically crosslinked poly(ethylene oxide) and ionic liquid, Eur. Polym. J. 44 (2008) 2986–2990.
[44] J.R. Nair, C. Gerbaldi, G. Meligrana, R. Bongiovanni, S. Bodoardo, N. Penazzi, P. Reale, V. Gentili, UV-cured methacrylic membranes as novel gel–polymer electrolyte for Li-ion batteries, J. Power Sour. 178 (2008) 751–757.
[45] C. Gerbaldi, J.R. Nair, S. Ahmad, G. Meligrana, R. Bongiovanni, S. Bodoardo, N. Penazzi, UV-cured polymer electrolytes encompassing hydrophobic room temperature ionic liquid for lithium batteries, J. Power Sour. 195 (2010) 1706–1713.
[46] C. Gerbaldi, J.R. Nair, G. Meligrana, R. Bongiovanni, S. Bodoardo, N. Penazzi, UV-curable siloxane-acrylate gel-copolymer electrolytes for lithium-based battery applications, Electrochim. Acta 55 (2010) 1460–1467.
[47] J.-.H. Baik, S. Kim, D.G. Hong, J.-.C. Lee, Gel Polymer electrolytes based on polymerizable Lithium salt and Poly(ethylene glycol) for Lithium battery applications, ACS Appl. Mater. Interf. 11 (2019) 29718–29724.
[48] S. Zugmann, M. Fleischmann, M. Amereller, R.M. Gschwind, H.D. Wiemhöfer, H.J. Gores, Measurement of transference numbers for lithium ion electrolytes via four different methods, a comparative study, Electrochim. Acta 56 (2011) 3926–3933.
[49] A.D. Becke, Density-functional thermochemistry. III. The role of exact exchange, J. Chem. Phys. 98 (1993) 5648–5652.
[50] Frisch, M.J., Trucks, G.W., Schlegel, H.B., Scuseria, G.E., Robb, M.A., Cheeseman, J.R., Scalmani, G., Barone, V., Petersson, G.A., Nakatsuji, H., Li, X., Caricato, M., Marenich, A.V., Bloino, J., Janesko, B.G., Gomperts, R., Mennucci, B., Hratchian, H.P., Ortiz, J.V., Izmaylov, A.F., Sonnenberg, J.L., Williams-Young, D., Ding, F., Lipparini, F., Egidi, F., Goings, J., Peng, B., Petrone, A., Henderson, T., Ranasinghe, D., Zakrzewski, V.G., Gao, J., Rega, N., Zheng, G., Liang, W., Hada, M., Ehara, M., Toyota, K., Fukuda, R., Hasegawa, J., Ishida, M., Nakajima, T., Honda, Y., Kitao, O., Nakai, H., Vreven, T., Throssell, K., Montgomery, J.A., Jr., Peralta, J.E., Ogliaro, F., Bearpark, M.J., Heyd, J.J., Brothers, E.N., Kudin, K.N., Staroverov, V.N., Keith, T.A., Kobayashi, R., Normand, J., Raghavachari, K., Rendell, A.P., Burant, J.C., Iyengar, S.S., Tomasi, J., Cossi, M., Millam, J.M., Klene, M., Adamo, C., Cammi, R., Ochterski, J.W., Martin, R.L., Morokuma, K., Farkas, O., Foresman, J.B., Fox, D.J.Gaussian, Inc., Wallingford CT, Gaussian 09, Revision D.01 (2016).
[51] Dennington, R., Keith, T.A., Millam, J.M., Semichem Inc., Shawnee Mission, KS, GaussView, Version 5 (2016).
[52] I.van der Veen, J. de Boer, Phosphorus flame retardants: properties, production, environmental occurrence, toxicity and analysis, Chemosphere 88 (2012) 1119–1153.
[53] C.-.T. Lin, S.-.W. Kuo, C.-.F. Huang, F.-.C. Chang, Glass transition temperature enhancement of PMMA through copolymerization with PMAAM and PTCM mediated by hydrogen bonding, Polymer 51 (2010) 883–889.
[54] M.H. Cohen, D. Turnbull, Molecular Transport in Liquids and Glasses, J. Chem. Phys. 31 (1959) 1164–1169.
[55] C.M. Hansen, in: The Three Dimensional Solubility Parameter, Danish Technical, Copenhagen, 1967, p. 14.
[56] A.F.M. Barton, CRC Handbook of Solubility Parameters and Other Cohesion Parameters, CRC press, 1991.
[57] J.Y. Song, Y.Y. Wang, C.C. Wan, Review of gel-type polymer electrolytes for lithium-ion batteries, J. Power Sour. 77 (1999) 183–197.
[58] A. Manuel Stephan, Review on gel polymer electrolytes for lithium batteries, Eur. Polym. J. 42 (2006) 21–42.
[59] X. Judez, M. Martinez-Ibañez, A. Santiago, M. Armand, H. Zhang, C. Li, Quasi-solid-state electrolytes for lithium sulfur batteries: advances and perspectives, J. Power Sour. 438 (2019) 226985.
[60] T. Nakano, S. Shimada, R. Saitoh, I. Noda, Transient 2D IR correlation spectroscopy of the photopolymerization of acrylic and epoxy monomers, Appl. Spectrosc. 47 (1993) 1337–1342.
[61] M. Orgill, B.L. Baker, N.L. Owen, FTIR studies of conformational isomerism in acrylates and acrylic acids, Spectrochimica Acta Part A 55 (1999) 1021–1024.
[62] S.J. Oh, S.C. Lee, S.Y. Park, Photopolymerization and photobleaching of n-butyl acrylate/fumed silica composites monitored by real time FTIR-ATR spectroscopy, Vib. Spectrosc. 42 (2006) 273–277.
[63] F. Bauer, U. Decker, S. Naumov, C. Riedel, Photoinitiator-free UV curing and matting of acrylate-based nanocomposite coatings: Part 3, Prog. Org. Coat. 77 (2014) 1085–1094.
[64] G. Zhou, H. Yao, Y. Zhou, W. Wang, M. Peng, Self-assembled complexes of graphene oxide and oxidized vapor-grown carbon fiber for simultaneously enhancing the strength and toughness of epoxy and multi-scale carbon fiber/epoxy composites, Carbon 137 (2018) 6–18.
[65] G. Zhou, W. Wang, M. Peng, Molecular-level dispersion of rigid-rod sulfonated aromatic polyamides in epoxy resin for extraordinary improvement in both strength and toughness, Polymer 163 (2019) 20–28.
[66] G. Zhou, W. Wang, M. Peng, Functionalized aramid nanofibers prepared by polymerization induced self-assembly for simultaneously reinforcing and toughening of epoxy and carbon fiber/epoxy multiscale composite, Compos. Sci. Technol. 168 (2018) 312–319.
[67] S. Wu, H. Zheng, R. Tian, Z. Hei, H. Liu, H. Duan, In-situ preparation of gel polymer electrolyte with glass fiber membrane for lithium batteries, J. Power Sour. 472 (2020) 228627.
[68] B. Weng, F. Xu, M. Alcoutlabi, Y. Mao, K. Lozano, Fibrous cellulose membrane mass produced via forcespinning® for lithium-ion battery separators, Cellulose 22 (2015) 1311–1320.
[69] M. Yanilmaz, M. Dirican, X. Zhang, Evaluation of electrospun SiO2/nylon 6,6 nanofiber membranes as a thermally-stable separator for lithium-ion batteries, Electrochim. Acta 133 (2014) 501–508.
[70] Y. Cui, J. Chai, H. Du, Y. Duan, G. Xie, Z. Liu, G. Cui, Facile and Reliable in Situ Polymerization of Poly(Ethyl Cyanoacrylate)-Based Polymer Electrolytes toward Flexible Lithium Batteries, ACS Appl. Mater. Interf. 9 (2017) 8737–8741.
[71] M. Liu, D. Zhou, Y.-.B. He, Y. Fu, X. Qin, C. Miao, H. Du, B. Li, Q.-.H. Yang, Z. Lin, T.S. Zhao, F. Kang, Novel gel polymer electrolyte for high-performance lithium–sulfur batteries, Nano Energy 22 (2016) 278–289.
[72] X. Li, S. Li, Z. Zhang, J. Huang, L. Yang, S.-i. Hirano, High-performance polymeric ionic liquid–silica hybrid ionogel electrolytes for lithium metal batteries, J. Mater. Chem. A 4 (2016) 13822–13829.
[73] J.-.H. Shin, W.A. Henderson, S. Passerini, PEO-based polymer electrolytes with ionic liquids and their use in Lithium metal-polymer electrolyte batteries, J. Electrochem. Soc. 152 (2005) A978–A983.
[74] J. Sunarso, Y. Shekibi, J. Efthimiadis, L. Jin, J.M. Pringle, A.F. Hollenkamp, D.R. MacFarlane, M. Forsyth, P.C. Howlett, Optimising organic ionic plastic crystal electrolyte for all solid-state and higher than ambient temperature lithium batteries, J. Solid State Electrochem 16 (2012) 1841–1848.
[75] B. Joos, T. Vranken, W. Marchal, M. Safari, M.K. Van Bael, A.T. Hardy, Eutectogels: a new class of solid composite electrolytes for Li/Li-ion batteries, Chem. Mater. 30 (2018) 655–662.
[76] Z. Zou, Y. Li, Z. Lu, D. Wang, Y. Cui, B. Guo, Y. Li, X. Liang, J. Feng, H. Li, C.-.W. Nan, M. Armand, L. Chen, K. Xu, S. Shi, Mobile ions in composite solids, Chem. Rev. (2020).
[77] Z. Lu, J. Yu, J. Wu, M.B. Effat, S.C.T. Kwok, Y. Lyu, M.M.F. Yuen, F. Ciucci, Enabling room-temperature solid-state lithium-metal batteries with fluoroethylene carbonate-modified plastic crystal interlayers, Energy Storage Mater. 18 (2019) 311–319.

[78] J. Yi, J. Chen, Z. Yang, Y. Dai, W. Li, J. Cui, F. Ciucci, Z. Lu, C. Yang, Facile patterning of laser-induced graphene with tailored Li nucleation kinetics for stable Lithium-metal batteries, Adv. Energy Mater. 9 (2019) 1901796.
[79] J. Chen, X. Fan, Q. Li, H. Yang, M.R. Khoshi, Y. Xu, S. Hwang, L. Chen, X. Ji, C. Yang, H. He, C. Wang, E. Garfunkel, D. Su, O. Borodin, C. Wang, Electrolyte design for LiF-rich solid–electrolyte interfaces to enable high-performance microsized alloy anodes for batteries, Nat. Energy 5 (2020) 386–397.
[80] L. Hu, Z. Zhang, K. Amine, Fluorinated electrolytes for Li-ion battery: an FEC-based electrolyte for high voltage LiNi0.5Mn1.5O4/graphite couple, Electrochem. Commun. 35 (2013) 76–79.
[81] C. Liu, Z.G. Neale, G. Cao, Understanding electrochemical potentials of cathode materials in rechargeable batteries, Mater. Today 19 (2016) 109–123.
[82] H.B. Son, M.-.Y. Jeong, J.-.G. Han, K. Kim, K.H. Kim, K.-.M. Jeong, N.-.S. Choi, Effect of reductive cyclic carbonate additives and linear carbonate co-solvents on fast chargeability of LiNi0.6Co0.2Mn0.2O2/graphite cells, J. Power Sources 400 (2018) 147–156.
[83] T. Jaumann, J. Balach, M. Klose, S. Oswald, U. Langklotz, A. Michaelis, J. Eckert, L. Giebeler, SEI-component formation on sub 5nm sized silicon nanoparticles in Li-ion batteries: the role of electrode preparation, FEC addition and binders, PCCP 17 (2015) 24956–24967.
[84] M.D. Bhatt, C. O'Dwyer, Solid electrolyte interphases at Li-ion battery graphitic anodes in propylene carbonate (PC)-based electrolytes containing FEC, LiBOB, and LiDFOB as additives, Chem. Phys. Lett. 618 (2015) 208–213.
[85] Y. Okuno, K. Ushirogata, K. Sodeyama, Y. Tateyama, Decomposition of the fluoroethylene carbonate additive and the glue effect of lithium fluoride products for the solid electrolyte interphase: an ab initio study, PCCP 18 (2016) 8643–8653.
[86] C.-.G. Zhan, J.A. Nichols, D.A. Dixon, Ionization potential, electron affinity, electronegativity, hardness, and electron excitation energy: molecular properties from density functional theory orbital energies, J. Phys. Chem. A 107 (2003) 4184–4195.
[87] J. Zheng, H. Zheng, R. Wang, L. Ben, W. Lu, L. Chen, L. Chen, H. Li, 3D visualization of inhomogeneous multi-layered structure and Young's modulus of the solid electrolyte interphase (SEI) on silicon anodes for lithium ion batteries, PCCP 16 (2014) 13229–13238.